JOURNAL OF SOLID STATE CHEMISTRY 105, 444–457 (1993)

Investigations on the Structural, Electrical and Magnetic Properties of Sr Substituted Ln_2NiO_4 (Ln = Pr, Sm, Gd)

S. C. CHEN, K. V. RAMANUJACHARY, AND MARTHA GREENBLATT*

Department of Chemistry, Rutgers, The State University of New Jersey, Piscataway, New Jersey 08855

Received August 27, 1992; in revised form November 9, 1992; accepted November 11, 1992

Solid solutions of $Ln_{2-x}Sr_xNiO_{4\pm\delta}$ (Ln = Pr, Sm) and $GdSrNiO_4$ were synthesized in air using conventional solid state methods and were characterized by powder X-ray diffraction, TGA, electrical resistivity, DSC, Seebeck coefficient, and magnetic susceptibility measurements. A structural transition from orthorhombic to tetragonal was observed at $x \sim 0.2$ for Pr and 0.8 for Sm. For both series of compounds (Ln = Pr, Sm), the tetragonal unit cell parameters a_t and c as functions of x display sharp minima and maxima, respectively, at $x \sim 0.6$. The tetragonality ratio, c/a_t, shows a maximum at $x \sim 0.6$. All the compounds are semiconducting from room temperature down to 25 K, except $SmSrNiO_4$ and $GdSrNiO_4$, which exhibit a degenerate semiconductor to semiconductor transition at ~292 K and ~260 K, respectively. Seebeck measurements indicate that electrons are the dominant carriers of conductivity at ambient temperature in all the compounds. The magnetic susceptibility data for all the samples, except $Sm_{2-x}Sr_xNiO_{4\pm\delta}$ for $x = 0.8$ and 1.0, follow Curie–Weiss behavior in the temperature range 100–300 K with no evidence of long range magnetic ordering. The effect of Sr^{2+} substitution on the structural, electrical, and magnetic properties of $Ln_{2-x}Sr_xNiO_{4\pm\delta}$ (Ln = Pr, Sm) is discussed in terms of the mixed-valent character of $Ni^{2+/3+}$ ions, the Ln–O vs Ni–O bond competition along the crystallographic c-axis, the size effect, the local distortion of NiO_6 octahedra, and a configurational transition in the d-manifold of nickel ions.

Introduction

Even before the discovery of superconductivity in the $La_{2-x}Ba_xCuO_4$ system (*1*), oxides crystallizing with the K_2NiF_4 structure (Fig. 1) were of interest, because of their interesting anisotropic transport properties (*2*). Special attention has been paid to La_2NiO_4 due to the possibility of approaching a transition from localized to itinerant $3d_{x^2-y^2}$ electrons of the Ni^{2+}. This transition may arise from strong Ni–O–Ni interactions due to the relatively short Ni–O bonds (1.93 Å) in the basal planes, compared to the corresponding distance of 2.089 Å in the binary NiO (*3*, *4*). As shown in Fig. 1, the structure of La_2NiO_4 can be described as an ordered intergrowth of perovskite $LaNiO_3$ and rock salt LaO layers stacked along the crystallographic c-axis. The NiO_6 octahedra share corners in the ab plane forming a two-dimensional network, which is responsible for a variety of interesting physical phenomena, for example, the anisotropic electrical transport and magnetic exchange interactions (*5–8*).

Compounds of $Ln_2NiO_{4+\delta}$ (Ln = La, Pr, Nd) show a considerable range of oxygen nonstoichiometry depending on the synthetic conditions. In a recent study, Jorgensen *et al.* have reported that the excess oxygen in $La_2NiO_{4+\delta}$, occupies the interstitial position $(\frac{1}{4}, \frac{1}{4}, \sim\frac{1}{4})$ (*9*). Recently, two types of homologous series of superstructures were observed in the oxygen rich compounds of $La_2NiO_{4+\delta}$ by transmission electron micros-

* To whom correspondence should be addressed.

0022-4596/93 $5.00

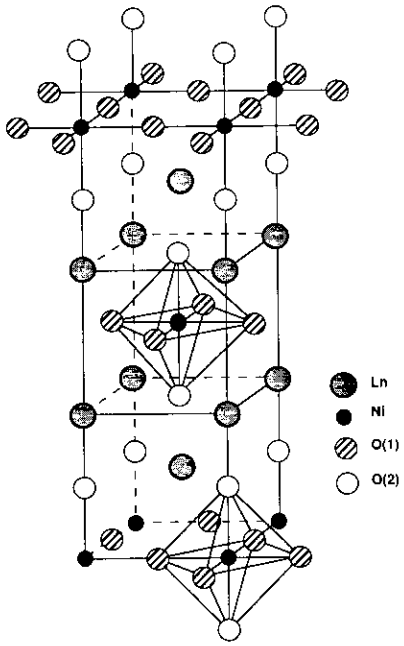

FIG. 1. Tetragonal K_2NiF_4-type structure of Ln_2NiO_4, Ln = La, Pr, Nd.

copy. The origin of these superstructures has been attributed to the ordering of the excess oxygen atoms (*10*). Furthermore, the structural and physical properties of these compounds have been reported to be extremely sensitive to oxygen stoichiometry (*6*, *8*, *11–14*). For example, nonstoichiometric $La_2NiO_{4+\delta}$ is tetragonal at ambient temperature, whereas nearly stoichiometric $La_2NiO_{4+\delta}$ ($\delta \sim 0$) shows orthorhombic distortions and long range magnetic ordering. In addition, the suppression of the magnetic ordering in $Nd_2NiO_{4+\delta}$ and $Pr_2NiO_{4+\delta}$ with increasing δ was reported by Buttrey and Honig (*8*).

Because of the similarities in the structures of La_2NiO_4 and La_2CuO_4 (the parent compound of the recently discovered high temperature superconducting cuprate family), as well as reports of possible superconductivity in $La_{2-x}Sr_xNiO_{4\pm\delta}$ (*15*), recently several studies have been carried out on the structural and physical properties of $Ln_{2-x}M_xNiO_{4\pm\delta}$ (Ln = trivalent rare earth ions, M = Ca, Sr, Ba) in order to better understand the nature of these rare earth nickelates, as well as that of the structurally related superconducting cuprates. Although a considerable number of studies have been reported on the structural, electrical, and magnetic properties of $Ln_{2-x}M_xNiO_{4\pm\delta}$ (Ln = La, Nd; M = Ca, Sr, Ba) (*16–21*), a systematic investigation with Ln = Pr, Sm, Gd has not yet been reported. We were also interested in the size effect of the rare earth ions on the solubility range of Sr^{2+} ion in $Ln_2NiO_{4+\delta}$ compounds. Therefore, a systematic study of the structural, electrical, and magnetic properties of $Ln_{2-x}Sr_xNiO_{4\pm\delta}$ (Ln = Pr, Sm, Gd) has been undertaken to investigate the effect of Sr substitution on the structural and physical properties in these systems.

Experimental

All the members of the Sr substituted Ln_2NiO_4 (Ln = Pr, Sm, Gd) were prepared in polycrystalline form by conventional solid state methods. Prior to use, Pr_6O_{11} or Ln_2O_3, Ln = Sm, Gd (Aldrich, 99.9%), was dried at 1100°C for 9 hr in air to remove any carbonate impurities; $Sr(NO_3)_2$ (Aldrich, 99+%) was dried at 160°C in a drying oven overnight. NiO (Aldrich, 99.99%) was used as obtained. Stoichiometric amounts of Ln_2O_3 (Ln = Sm, Gd) or Pr_6O_{11}, $Sr(NO_3)_2$ and NiO were thoroughly ground together and calcined in air at 800°C in alumina crucibles for 9 hr to decompose the nitrates. The resulting black powders were then reground and heated in air at 1300°C in the same crucibles for 4 days, usually with one intermittent grinding. The samples were cooled to 800°C in the furnace before being quenched to room temperature. The powders were finally cold pressed (~25 klb/in^2) into pellets and sintered in air at 1300°C for an additional period of 24 hr. These pellets were later used for all the measurements reported.

Powder X-ray diffraction (PXD) data collected on a SCINTAG PAD V diffractometer with filtered Cu$K\alpha$ radiation were

used to monitor the completion of the reaction. The high temperature X-ray structural investigations were carried out in a similar diffractometer equipped with a hot stage. Least-squares refinement of the observed powder diffraction data in the range of $10° \leq 2\theta \leq 80°$ was used to evaluate the unit cell parameters. National Bureau of Standards silicon powder (NBS-640B) was used as an internal standard. The total oxygen content of the samples was determined by hydrogen reduction in a DuPont 951 Thermogravimetric Analyzer (TGA); the material was heated in a platinum pan, in flowing 5% H_2 in helium gas (flow rate = 150 ml/min), to 900°C at a rate of 10°C/min.

Electrical resistivity measurements, in the temperature range 25–300 K, were carried out on sintered pressed pellets, by a standard four-probe technique with a DE 202 cryostat (APD cryogenics). The Seebeck coefficients were estimated by applying a thermal gradient ($\Delta T < 3$ K) across the pellet while measuring the potential difference (ΔV) between two ends of the pellet with a Nanovoltmeter (Kethley Model 180). The high temperature resistivity measurements were carried out in a standard two-probe configuration. The DSC measurements were made with a DuPont Differential Scanning Calorimeter (Model 910) in the temperature range 210–773 K on 20 mg samples; a heating rate of 5°C/min was used. A SQUID magnetometer (MPMS, Quantum Design) was used to measure the magnetic susceptibility of sintered pellets in the temperature range 5–370 K at an applied field of 1000 G.

Results and Discussion

Structural Properties

The preparation of the solid solutions $Ln_{2-x}Sr_xNiO_{4\pm\delta}$ (*Ln* = Pr, Sm, Gd) was attempted in the range $0.0 \leq x \leq 1.0$. The formation of X-ray pure single phase specimens in these series is observed when x = 0.0–1.0 for Pr and 0.5–1.0 for Sm. For $Gd_{2-x}Sr_xNiO_{4\pm\delta}$, single phase composition is achieved only with $x = 1.0$. $SrLn_2O_4$, Ln_2O_3 (Sm, Gd), and NiO were commonly observed impurities for $x < 0.5$ for Sm and $x < 1.0$ for Gd. It is known that under normal conditions the K_2NiF_4 structure is not stable for Ln_2NiO_4 with small rare earth ions, so Sm_2NiO_4 and Gd_2NiO_4 have never been prepared. Thus the results presented show that Sr incorporation in the *Ln*O sublattice stabilizes the K_2NiF_4 structure for the small rare earth ions; the smaller the rare earth ion, the greater is the Sr content required to stabilize the K_2NiF_4-type phase.

It has been reported that $LnSrNiO_4$ (*Ln* = La, Nd, Sm, Eu, Gd) (*22*) adopts the tetragonal K_2NiF_4-type structure, whereas $Ln_2NiO_{4+\delta}$ (*Ln* = La, Nd) (9, *23*) crystallizes with an orthorhombically distorted structure. A recent neutron scattering study on the structure of nonstoichiometric $Pr_2NiO_{4+\delta}$ revealed that this compound is either tetragonal or orthorhombic, depending on the oxygen content of the samples (*11*). $LnSrNiO_4$ (*Ln* = Pr, Sm, Gd) and $Pr_2NiO_{4.09}$ prepared in this investigation are indexed as tetragonal (S.G. *I4/mmm*) and orthorhombic (S.G. *Bmab*), respectively. The orthorhombic distortion of the K_2NiF_4 structure manifests itself by the splitting of some of the *hk*0-type reflections in the powder X-ray diffraction patterns. The degree of divergence in the *hk*0 reflections served as an indicator of the degree of distortion from the ideal tetragonal geometry. The splitting of the *hk*0 peaks in the PXD of $Pr_{2-x}Sr_xNiO_{4\pm\delta}$ was observed for $x < 0.2$, and for $x < 0.8$ in $Sm_{2-x}Sr_xNiO_{4\pm\delta}$. However, no observable splitting of the *hk*0 class of reflections in the range $10° \leq 2\theta \leq 80°$ was found for $x \geq 0.2$ in $Pr_{2-x}Sr_xNiO_{4\pm\delta}$ and $x \geq 0.8$ in $Sm_{2-x}Sr_xNiO_{4\pm\delta}$. This observation suggests that a structural transition from orthorhombic to tetragonal symmetry (O–T) in $Pr_{2-x}Sr_xNiO_{4\pm\delta}$ and $Sm_{2-x}Sr_xNiO_{4\pm\delta}$ occurs at $x \sim 0.2$ and 0.8, respectively. The overall oxygen contents, unit cell parameters, O–T structural transition temperatures (T_1), and metal–semiconductor transition temperatures (T_2) of the

TABLE I

UNIT CELL PARAMETERS OF Sr-SUBSTITUTED $Ln_{2-x}Sr_xNiO_{4\pm\delta}$ (*Ln* = Pr, Sm, Gd)

Compound	*a* (Å)	*b* (Å)	*c* (Å)	Volume (Å)^3	c/a_t	T_1 (°C)[a]	T_2 (°C)[b]
$Pr_2NiO_{4.09\pm0.003}$	5.3965(6)	5.4538(7)	12.434(1)	365.96(5)		565(5)	347(2)
	(3.8362)[c]			(182.984)[d]	(3.241)[d]		
$Pr_{1.9}Sr_{0.1}NiO_{4.09\pm0.003}$	5.3902(7)	5.4296(7)	12.452(1)	364.43(5)		300(5)	334(2)
	(3.8254)[c]			(182.219)[d]	(3.2551)[d]		
$Pr_{1.8}Sr_{0.2}NiO_{4.04\pm0.003}$	3.8160(3)		12.468(2)	181.56(3)	3.267		255(8)
$Pr_{1.6}Sr_{0.4}NiO_{4.04\pm0.003}$	3.7970(3)		12.512(2)	180.38(2)	3.295		245(8)
$Pr_{1.5}Sr_{0.5}NiO_{3.99\pm0.003}$	3.7850(3)		12.550(2)	179.72(3)	3.316		228(8)
$Pr_{1.4}Sr_{0.6}NiO_{3.99\pm0.003}$	3.7836(2)		12.5435(7)	179.57(2)	3.315		205(8)
$Pr_{1.2}Sr_{0.8}NiO_{3.99\pm0.003}$	3.7895(4)		12.466(2)	179.01(3)	3.290		130(8)
$PrSrNiO_{3.96}$	3.7972(3)		12.410(2)	178.93(3)	3.268		50(8)
$Sm_{1.5}Sr_{0.5}NiO_{3.98\pm0.003}$	5.3089(9)	5.366(1)	12.331(2)	351.31(7)		613(5)	
	(3.774)[c]			(175.65)[d]	(3.267)[d]		
$Sm_{1.4}Sr_{0.6}NiO_{4.01\pm0.003}$	5.3158(3)	5.3407(6)	12.3467(4)	350.52(5)		567(5)	
	(3.7676)[c]			(175.26)[d]	(3.277)[d]		
$Sm_{1.2}Sr_{0.8}NiO_{3.99\pm0.003}$	3.7667(3)		12.318(2)	174.77(3)	3.270		
$SmSrNiO_{3.97\pm0.003}$	3.7804(3)		12.256(1)	175.16(3)	3.242		
$GdSrNiO_{3.96\pm0.003}$	3.7652(2)		12.2057(8)	173.03(2)	3.242		

[a] Structural phase transition temperatures estimated from high temperature X-ray diffraction study.

[b] Metal–semiconductor transition temperatures estimated from both high temperature resistivity and DSC measurements ($x \approx 0.0$ and 0.1) and from DSC measurements alone ($x = 0.2 \sim 1.0$).

[c] The a_t for the orthorhombic samples were calculated using the expression $a_t = (a + b)/2\sqrt{2}$.

[d] Values for the orthorhombic samples were calculated using a_t instead of *a*.

samples in the single phase region of $Ln_{2-x}Sr_xNiO_{4\pm\delta}$ (*Ln* = Pr, Sm, Gd) are listed in Table I. These data show that a rapid compression of the *b* unit cell parameter occurs at the orthorhombic to tetragonal phase transition in $Ln_{2-x}Sr_xNiO_{4\pm\delta}$ (*Ln* = Pr, Sm), while the *a* unit cell parameter remains nearly constant.

The oxygen contents of the samples were determined by TGA studies under a hydrogen atmosphere. The total oxygen stoichiometries were estimated from the integrated peak intensities of the first derivatives of the weight changes with Ln_2O_3, SrO, and Ni as final products. As shown in Table I, the oxygen content of the $Pr_{2-x}Sr_xNiO_{4\pm\delta}$ solid solutions remains close to the ideal value of 4 for the tetragonal compositions, while significant deviations from 4 were observed in the orthorhombic compositions. This indicates that the orthorhombically distorted K_2NiF_4-type structure in $Pr_{2-x}Sr_xNiO_{4\pm\delta}$ ($x < 0.2$), which most likely arises from the mismatch between the NiO_2 and the $Pr_{2-x}Sr_xO_{2+\delta}$ layers, is stabilized by the incorporation of extra oxygens in the structure. Similar effects of oxygen stoichiometry were also observed in $Nd_{2-x}Sr_xNiO_{4\pm\delta}$ (*19*); however, the tetragonal structure ($x > 0.2$) is stabilized with higher Sr^{2+} and Ni^{3+} content in the Pr^{3+} phase. In general, the amount of excess oxygen (δ) in $Ln_2NiO_{4+\delta}$ (*Ln* = La, Pr, Nd) appears to increase with decreasing size of the rare earth ion; for example, $\delta \sim 0.04$ for La (*17*), 0.09 for Pr, and 0.16 for Nd (*19*). In contrast, oxygen contents close to the stoichiometric value ($\delta \sim 0$) are seen in orthorhombic structures of $Sm_{2-x}Sr_xNiO_{4\pm\delta}$, albeit with considerably higher Sr contents ($x = 0.5$ and 0.6); this trend implies that extra oxygens ($\delta > 0$) are not required for the stabilization of the K_2NiF_4 structure with an orthorhombic distortion.

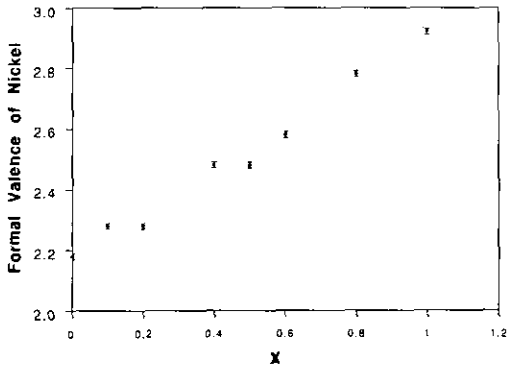

FIG. 2. Formal valence of nickel ion as a function of Sr content in $Pr_{2-x}Sr_xNiO_{4\pm\delta}$.

In the case of $Ln_{2-x}Sr_xNiO_{4\pm\delta}$ with Ln = Sm, Gd, the apparent instability of compounds with $x < 0.5$ for Sm and $x < 0.8$ for Gd implies that the size of the interstitial site created by tilting the NiO_6 octahedra (*8*) may be too small to permit the incorporation of the extra oxygen atoms, owing to the relatively smaller unit cell size. Thus a high Sr content is usually required to stabilize the K_2NiF_4 type structure in $Ln_{2-x}Sr_xNiO_{4\pm\delta}$ (Ln = Sm, Gd). These arguments are consistent with the tolerance factor consideration to be discussed later.

Figure 2 shows that in $Pr_{2-x}Sr_xNiO_{4\pm\delta}$ ($0 < x < 1$) the formal valence of nickel ion (estimated from oxygen content analysis) increases nearly monotonically with the Sr content. The variation of the unit cell parameters a_t (a_t for the orthorhombic samples were calculated from the expression $a_t = (a + b)/2\sqrt{2}$), c, volume, and the tetragonality ratio, c/a_t, with x for $Ln_{2-x}Sr_xNiO_{4\pm\delta}$ (Ln = Pr, Sm) are illustrated in Figs. 3a–3d, respectively. The tetragonality ratio, c/a_t, and the unit cell parameters (a_t, c, and volume) decrease with decreasing size of the rare earth ion (Figs. 3a–3d, Table I). In each solid solution (Ln = Pr, Sm), the variation of the unit cell parameters with x displays a sharp minimum in a_t and a maximum in c at $x \sim 0.6$; consequently, c/a_t shows a maximum at $x \sim 0.6$. These trends are essentially the same as those observed for $Ln_{2-x}M_xNiO_{4\pm\delta}$ (Ln = La, Nd; M = Ca, Sr, Ba) (*16–21*). Gopalakrishnan *et al.* (*16*), in their study of $La_{2-x}Sr_xNiO_{4\pm\delta}$, attributed the initial increase of c/a_t for samples with $0 \le x \le 0.5$ to the Jahn–Teller distortion of the NiO_6 octahedra with increasing Ni^{3+} concentration. They interpreted the decrease in c/a_t for samples with $x > 0.5$ in terms of a crossover in the electronic configuration of Ni^{3+} ions from $t_{2g}^6 d_{z^2}^1 d_{x^2-y^2}^0$ to $t_{2g}^6 d_{x^2-y^2}^1 d_{z^2}^0$.

Recently, a Rietveld analysis of the room temperature PXD data of $La_{2-x}Sr_xNiO_{4\pm\delta}$ (*17*) indicated that a maximum in c/a_t appeared at $x \sim 0.6$, while distortion of the NiO_6 octahedron, Ni–O(2) ($\|c$-axis)/Ni–O(1) ($\|a$-axis), decreased monotonically with increasing x for $0.0 \le x \le 1.4$. In addition, the Ni–O(1) ($\|a$-axis) bond length displayed a minimum at $x \sim 0.6$; the Ni–O(2) ($\|c$-axis) bond length generally decreased with increasing x, but more rapidly at $x \sim 0.6$. The La(Sr)–O(2) ($\|c$-axis) bond length, on the other hand, continuously increased with increasing x for $0.0 \le x \le 1.4$. These results do not support the Jahn–Teller enhancement of the NiO_6 octahedral distortion along the crystallographic c-axis with increasing Ni^{3+} concentration as previously suggested (*16*, *19*). The possibility of a transition from $t_{2g}^6 d_{z^2}^1 d_{x^2-y^2}^0$ to $t_{2g}^6 d_{x^2-y^2}^1 d_{z^2}^0$ at the Ni^{3+} ions was excluded by Takeda *et al.* (*17*) who left the origin of the observed anomalous behavior in the unit cell parameters at $x \sim 0.6$ unanswered.

In this study we made an attempt to rationalize the observed anomalous variations in the unit cell parameters at $x \sim 0.6$ in terms of (a) a bond competition along the c-axis, (b) size effects, (c) a configurational transition in the d-manifold of the Ni^{3+} ion, and (d) the Jahn–Teller distortion of Ni^{3+} ion. As shown in Fig. 1, the Ln(Sr) and O(2) atoms are located at special positions 4*e* with coordinates (0, 0, z), the Ni atoms at (0, 0, 0) in sites 2*a*, and the O(1) atoms at ($\frac{1}{2}$, 0, 0), (0, $\frac{1}{2}$, 0) in sites 4*c* of space group *I*4/*mmm* (*24*). The local distortion of the NiO_6 octahedron along the c-axis depends

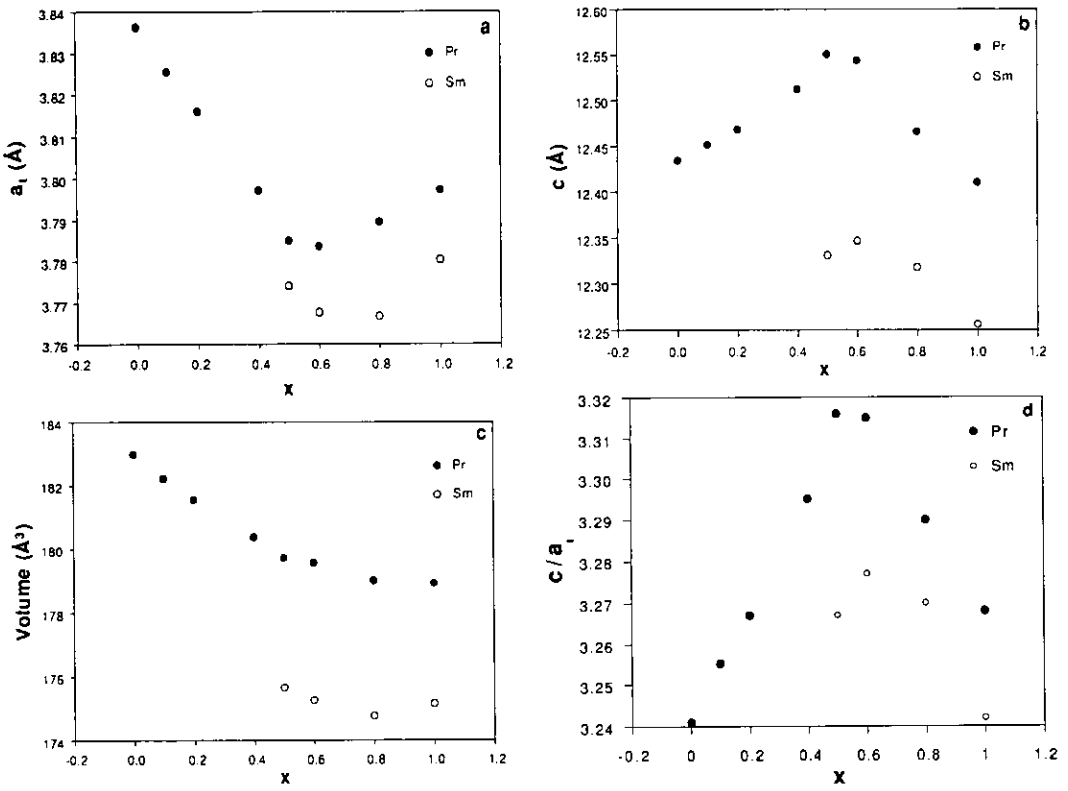

FIG. 3. (a) Variation of lattice parameter a_t, (b) variation of lattice parameter c, (c) variation of unit cell volume, and (d) variation of the tetragonality ratio, c/a_t, in $Pr_{2-x}Sr_xNiO_{4\pm\delta}$ and $Sm_{2x}Sr_xNiO_{4\pm\delta}$ as a function of Sr content. Errors in the unit cell parameters are presented in Table I.

closely on the relative bond strengths of the Ln(Sr)–O(2) and Ni–O(2) bonds along the tetragonal c-axis. The strong ionic character of the Ln(Sr)–O(2) bond is expected to weaken and consequently stretch the Ni–O(2) bond along the c-axis. A similar bond competition along the c-axis has been previously suggested in some compounds with the K_2NiF_4 type structure (*25*, *26*). In $Ln_{2-x}Sr_xNiO_4$, the Ni^{3+} content increases with increasing x. With increasing Ni^{3+} content, one would expect an increasing distortion of the NiO_6 octahedra due to implications of the Jahn–Teller effect, and as a result the Ni–O(2) distance should increase with increasing x. In fact, one observes a continuous decrease of Ni–O(2) distance and a progressive increase of La(Sr)–O(2) distance with increasing x in $La_{2-x}Sr_xNiO_4$ (*17*). These observed trends in the bond lengths of Ni–O(2) and La(Sr)–O(2), as well as the increase of c cell parameter up to $x \sim 0.6$, may be attributed to: (a) a bond competition along the c-axis and (b) size effects. In general, the Ln(Sr)–O(2) distance and the c-axis are lengthened by Sr substitution both because of the relatively large size of Sr, relative to Ln, and because the Sr–O(2) bond is less polar than the La–O(2) bond. This latter effect leaves more of the electron density for Ni–O(2) covalent interaction, and a shorter Ni–O(2) bond is observed. It appears that the effects of the Jahn–Teller distortion on the NiO_6 octahedra are suppressed by the concommitent shortening of the Ni–O(2) bond length due

to enhanced covalent interaction with increasing x.

The decrease of the c cell parameter for $x > 0.6$, may be explained in terms of the shortening of Ni–O(2) bond length as a result of a crossover transition of $t_{2g}^6 d_{z^2}^1 d_{x^2-y^2}^0$ to $t_{2g}^6 d_{x^2-y^2}^1 d_{z^2}^0$ configuration at the Ni^{3+} ions. This in turn more than compensates the expected elongation of La(Sr)–O(2) bond distance with increasing x. This configurational change in the d-manifold of Ni^{3+} ions is also supported by the increase of the a cell parameter or Ni–O(1) bond length for $x > 0.6$ in $Ln_{2-x}Sr_xNiO_{4\pm\delta}$ (Fig. 1). The observation of a sharp minimum at $x \sim 0.6$ in both the a cell parameter and the Ni–O(1) bond length is, therefore, strong evidence for a $t_{2g}^6 d_{z^2}^1 d_{x^2-y^2}^0$ to $t_{2g}^6 d_{x^2-y^2}^1 d_{z^2}^0$ configurational crossover at the Ni^{3+} ions. Moreover, the observation of a sharp minimum at $x \sim 0.6$ in the bond length of La(Sr)–O(2) ($\|[110]$) in $La_{2-x}Sr_xNiO_{4\pm\delta}$ (*17*) further supports this configurational transition at the Ni^{3+} ions. However, the transition may not be complete even at $x = 1.0$, where the bond length of Ni–O(2) is still slightly longer than that of Ni–O(1) (*17*).

As shown in Fig. 3c, the reduction of the unit cell volume across the series from $0.0 \leq x \leq 1.0$ in $Pr_{2-x}Sr_xNiO_{4\pm\delta}$ and $0.5 \leq x \leq 0.8$ in $Sm_{2-x}Sr_xNiO_{4\pm\delta}$ is presumably related to the partial oxidation of Ni^{2+} ($r_{Ni^{2+}} = 0.83$ Å for C.N. = 6) to Ni^{3+} ($r_{Ni^{3+}} = 0.70$ Å for C.N. = 6, low spin case) induced by the substitution of Sr^{2+} for Pr^{3+} (or Sm^{3+}). Apparently, the one-dimensional elongation along the c-axis expected from the difference of ionic radii of Sr^{2+} ($r_{Sr^{2+}} = 1.45$ Å for C.N. = 9) and Pr^{3+} (or Sm^{3+}) ($r_{Pr^{3+}} = 1.319$ Å, $r_{Sm^{3+}} = 1.272$ Å for C.N. = 9) (*27*) is not large enough to completely compensate the two-dimensional compression in the ab-plane caused by the partial oxidation of Ni^{2+} to Ni^{3+} ions. The reason for a larger unit cell volume of $SmSrNiO_4$, relative to the other members in the $Sm_{2-x}Sr_xNiO_{4\pm\delta}$ series is not clear at present. The unit cell parameters of $SmSrNiO_{3.97}$ (Table I) are, however, consistent with the data (a = 3.777(5) Å, c = 12.25(2) Å) previously reported by Demazeau *et al.* (*22*).

Saez-Puche *et al.* reported the observation of a structural transition from orthorhombic to tetragonal in nonstoichiometric $Pr_2NiO_{4+\delta}$ at 834 K (*28*). In order to understand the influence of Sr^{2+} substitution on the nature of this phase transition, we have carried out high temperature powder X-ray diffraction studies in air and these results are presented in Table I. We observed that the incorporation of Sr^{2+} into $Pr_2NiO_{4.09}$ leads to a dramatic decrease in the orthorhombic to tetragonal transition temperature. In contrast, the decrease in the transition temperature for $Sm_{2-x}Sr_xNiO_{4\pm\delta}$ with x from 0.5 to 0.6 is not as significant. The lowering of this structural transition temperature with the increase of Sr^{2+} content, which has also been observed in $Nd_{2-x}Sr_xNiO_{4\pm\delta}$ (*19*), may be understood in terms of the tolerance factor for the K_2NiF_4 structure. The stability of the A_2BO_4 structure is often described in terms of a tolerance factor defined as (*29*)

$$t = (r_A + r_O)/\sqrt{2}(r_B + r_O),$$

where $r_A + r_O$ and $r_B + r_O$ refer to the sum of the ionic radii of A–O and B–O bonds in nine and six coordinations, respectively. The K_2NiF_4 structure appears to be stable over the range $0.866 < t < 1.0$ (*30*). Based on Shannon's ionic radii (*27*), the calculated tolerance factors of orthorhombic compositions are 0.881 and 0.89 for $Pr_{2-x}Sr_xNiO_{4\pm\delta}$ (x = 0.0 and 0.1); 0.895 and 0.903 for $Sm_{2-x}Sr_xNiO_{4\pm\delta}$ (x = 0.5 and 0.6). These values are close to the lower limit of the structural stability of the K_2NiF_4 type, consistent with the observed structural distortions from the ideal tetragonal geometry. The increase of the tolerance factor (t) with increasing Sr content also explains the concomitant lowering of the orthorhombic-to-tetragonal transition temperatures. The upper limit tolerance factor calculated for $GdSrNiO_4$ is 0.922. Based on tolerance factor considerations alone, one would expect a wider range of Sr substitution in

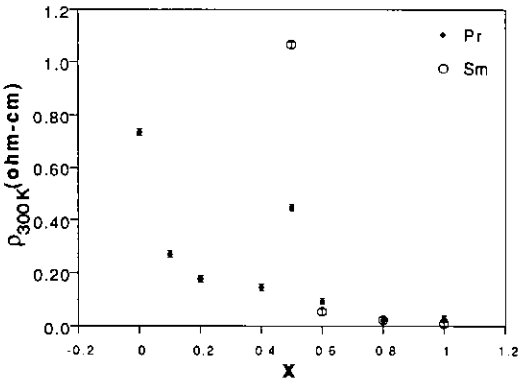

FIG. 4. Variation of the room temperature electrical resistivity as a function of Sr content in $Pr_{2-x}Sr_xNiO_{4\pm\delta}$ and $Sm_{2-x}Sr_xNiO_{4\pm\delta}$.

$Gd_{2-x}Sr_xNiO_{4\pm\delta}$ for $x < 1.0$. Possibly the use of more reactive starting materials or higher preparative temperatures may help to extend the Sr substitution range in this system, although factors other than the tolerance factor may also play an important role in the structural stability.

Electrical Properties

The room temperature resistivities (ρ_{RT}) as a function of x are plotted in Fig. 4, and show that the electrical resistivity decreases with increasing x in $Ln_{2-x}Sr_xNiO_{4\pm\delta}$ (Ln = Pr, Sm). The decrease in ρ_{RT} correlates well with the increasing ratio of Ni^{3+}/Ni^{2+}, induced by the progressive replacement of Sr^{2+} for Ln^{3+} (Fig. 2). To a first approximation the electrical conductivity can be expressed in terms of the number (n), mobility (μ), and charge (e) of the carriers according to the equation

$$\sigma = n\mu e.$$

The incorporation of Sr^{2+} in place of the trivalent rare earth ions in the Ln_2NiO_4 structure would result in (a) the increase of the number of carriers, due to the increase of the Ni^{3+}/Ni^{2+} ratio, and (b) the increase of the mobility of the carriers, resulting from the increase in the overlap of orbital wave functions on adjacent Ni atoms through the oxide ion intermediacy in the basal planes. Based on tolerance factor considerations, the substitution of Sr^{2+} for Ln^{3+} cations in these solid solutions would reduce the structural distortions between neighboring NiO_6 octahedra leading to a bond angle of Ni–O–Ni in the *ab* plane close to 180°, which would in turn increase the overlap of orbital wave functions on adjacent Ni atoms. These results are in agreement with the observed increase in the electrical conductivity.

An anomalously high room temperature resistivity was, however, observed for the compositions with Ni^{3+}/Ni^{2+} ratio of approximately 0.5, namely $Pr_{1.5}Sr_{0.5}NiO_4$ and $Sm_{1.5}Sr_{0.5}NiO_4$. Similar anomalous behavior in the transport properties was also observed in $La_{1.5}Sr_{0.5}NiO_4$ (*17*) and $Nd_{1.5}Sr_{0.5}NiO_4$ (*19*, *20*). The reason for this anomaly is not clear yet; it is possible that a charge ordering may take place at the Ni site, which in turn creates an additional potential that impedes the flow of the carriers. If a charge ordering of nickel ions is indeed responsible for this anomaly, we expect to see superstructure in these compounds. In a recent study on the crystal and magnetic structures of $Nd_{1.5}Sr_{0.5}NiO_4$ by neutron diffraction, no evidence of a long range superstructure was observed (*31*). Electron diffraction and transmission electron microscopy studies

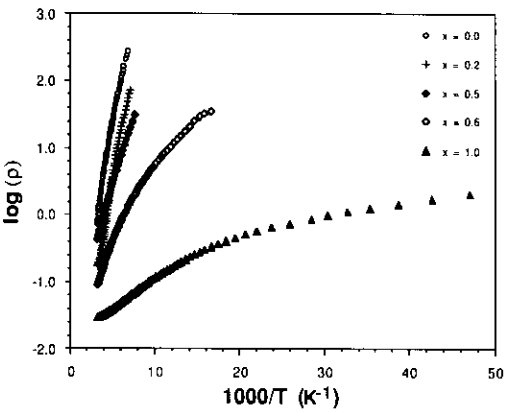

FIG. 5. Inverse temperature dependence of log(ρ) for x = 0.0, 0.2, 0.5, 0.6, and 1.0 in $Pr_{2-x}Sr_xNiO_{4\pm\delta}$.

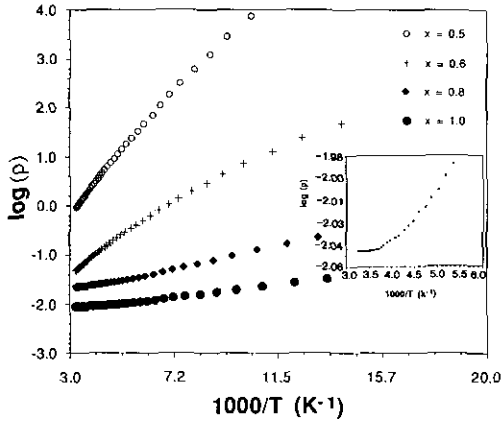

FIG. 6. Inverse temperature dependence of log(ρ) for $x = 0.5$, 0.6, 0.8, and 1.0 in $Sm_{2-x}Sr_xNiO_{4\pm\delta}$. The inset shows the degenerate semiconductor to semiconductor transition at ~292 K for sample with $x = 1.0$.

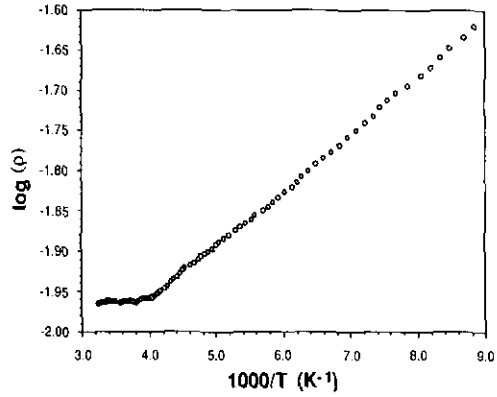

FIG. 7. Inverse temperature dependence of log(ρ) for $GdSrNiO_4$ showing the degenerate semiconductor to semiconductor transition at ~260 K.

on $Ln_{1.5}Sr_{0.5}NiO_4$ (Ln = La, Pr, Nd, or Sm) may give information on ordered structures. If the structural ordering is short ranged (which may be the case in these compounds), electron diffraction techniques should be advantageous over X-ray and neutron diffraction methods, which detect the averaged structure. Moreover, in view of the transport anisotropy associated with the K_2NiF_4-type oxides, the electrical resistivities of sintered pressed pellets represent only the average value of different orientation rather than the absolute value. Further investigations are therefore needed, especially on the structural and physical properties of single crystals of $Ln_{1.5}Sr_{0.5}NiO_4$ (Ln = La, Pr, Nd, Sm).

The variation of log ρ vs $1/T$ for selected samples of $Pr_{2-x}Sr_xNiO_{4\pm\delta}$ and $Sm_{2-x}Sr_xNiO_{4\pm\delta}$ measured in the temperature range 25–300 K is presented in Figs. 5 and 6, respectively. The electrical resistivity data of $GdSrNiO_4$ is presented in Fig. 7. All the members of these solid solution series are semiconducting down to 25 K, except for $SmSrNiO_4$ (see inset in Fig. 6) and $GdSrNiO_4$, which undergo a degenerate semiconductor to semiconductor transition at 292 ± 2 and 260 ± 2 K, respectively. Figure 8 shows that the activation energy estimated from the plot of log ρ vs $1/T$ in the temperature range 150–250 K decreases with increasing x across the series, except for $Pr_2NiO_{4.09}$ whose activation energy (0.13 eV) is somewhat lower than that of $Pr_{1.9}Sr_{0.1}NiO_{4.09}$ (0.15 eV). This decrease in the activation energy with increasing x across the series appears to indicate an increased delocalization of the Ni^{2+}/Ni^{3+} electrons in the basal planes. The dramatic reduction in the activation energy in the $0.4 < x < 0.6$ region is consistent with the crossover transition of $t_{2g}^6 d_{z^2}^1 d_{x^2-y^2}^0$ to $t_{2g}^6 d_{x^2-y^2}^1 d_{z^2}^0$ on the Ni^{3+} ion at $x \sim 0.6$ suggested earlier. As suggested by Takeda *et al.*

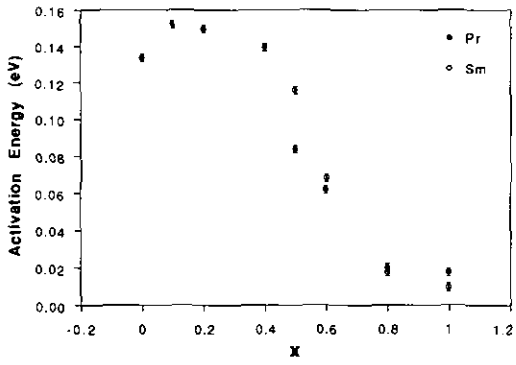

FIG. 8. Variation of the activation energy as a function of Sr content in $Pr_{2-x}Sr_xNiO_{4\pm\delta}$ and $Sm_{2-x}Sr_xNiO_{4\pm\delta}$.

(*20*), this configurational change is probably not sharp but leads to a gradual upward shift of the $d_{z^2}^1$ level with increasing x, such that the residual electrons tend to occupy the $\sigma^*_{x^2-y^2}$ band in preference to the d_{z^2} level. The decrease in electron density and the preferred population of $\sigma^*_{x^2-y^2}$ band would tend to reduce the correlation splitting of $\sigma^*_{x^2-y^2}$ band and gradually lead from localized to itinerant electronic behavior. The decreasing slope of log ρ vs $1/T$ seen at low temperatures (Figs. 5 and 6) can be explained in terms of extrinsic effects on the transport properties. A similar behavior of log ρ vs $1/T$ was also observed in $Nd_{2-x}Sr_xNiO_{4\pm\delta}$ (*19*).

To better understand the influence of Sr substitution on the nature of electrical transport properties, we have extended the temperature range for resistivity measurements to higher temperatures and also carried out DSC studies on the $Pr_{2-x}Sr_xNiO_{4\pm\delta}$ system. As shown in Table I, the sharp decrease in the metal-to-semiconductor transition temperature across the structural transition from orthorhombic (x = 0.1) to tetragonal (x = 0.2) system could be explained in terms of the structural distortions between neighboring NiO_6 octahedra in the orthorhombic compositions, which results in the bending of the Ni–O–Ni bond angles in the *ab* plane away from 180° (*11*). The bending of the Ni–O–Ni bond angle would reduce the orbital overlap between Ni ions, a requirement for an effective delocalization of carriers in these compounds. The Seebeck effect indicates that at room temperature, electrons are the dominant carriers in all the compounds reported here.

Magnetic Properties

Figure 9 shows the variation of the magnetic susceptibility with temperature in the range 2–300 K for selected members in $Pr_{2-x}Sr_xNiO_{4\pm\delta}$. The susceptibility values were not corrected for the temperature independent terms (χ_0) because of the large paramagnetic contribution from the rare earth ions. From the magnetic susceptibility data

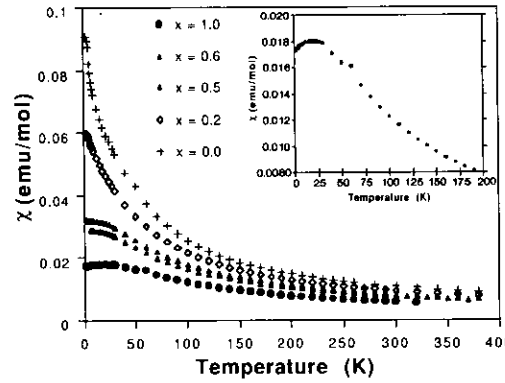

FIG. 9. Temperature dependence of magnetic susceptibility for x = 0.0, 0.2, 0.5, 0.6, and 1.0 in $Pr_{2-x}Sr_xNiO_{4\pm\delta}$. The inset shows χ vs T for $PrSrNiO_4$ in the temperature range 2–200 K illustrating the saturation of χ below 30 K.

analysis, no evidence for a long range magnetic order of either Pr^{3+} (Sm^{3+}, Gd^{3+}) or $Ni^{2+/3+}$ moments down to 2 K was observed in any of the compounds. The absence of a long range magnetic order in $Pr_2NiO_{4.09}$ is consistent with the observations of Buttrey and Honig (*8*), who showed that the magnetic order of the nickel sublattice can be suppressed with large excess of oxygen in the structure. As shown in Fig. 9, the nearly invariant behavior of χ below 30 K observed for $Pr_{2-x}Sr_xNiO_{4\pm\delta}$ ($0.5 \leq x \leq 1.0$) most likely arises from the depopulation of high energy states in the Pr^{3+} moments by the crystal electric field (CEF) resulting in a singlet ground state. This behavior has also been reported for several compounds containing Pr^{3+} ions, including Pr_2CuO_{4-y} (*32*) and $PrSrVO_4$ (*33*). The origin of the downturn in magnetic susceptibility of $PrSrNiO_4$ at $T < 9$ K, as shown in the inset of Fig. 9, is not clear at this point; however, a short range weak antiferromagnetic coupling might be responsible due to exchange interactions of the type J_{Pr-Pr}, J_{Pr-Ni}, or J_{Ni-Ni}.

The susceptibility data of $Pr_{2-x}Sr_xNiO_{4\pm\delta}$ in the temperature range 100 ~ 300 K can be fit to the Curie–Weiss equation

$$\chi = C/(T - \Theta),$$

where C and Θ are the Curie and Weiss

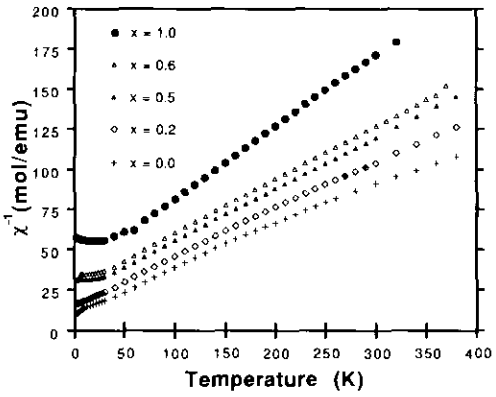

FIG. 10. Variation of inverse susceptibility with temperature for $x = 0.0$, 0.2, 0.5, 0.6, and 1.0 in $Pr_{2-x}Sr_xNiO_{4\pm\delta}$.

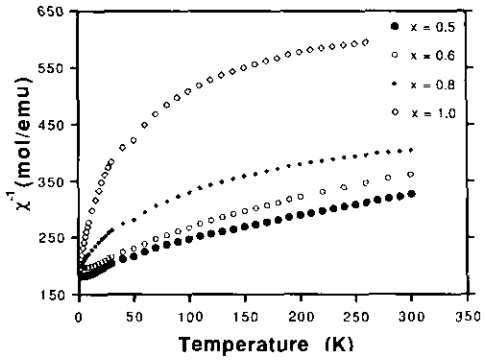

FIG. 11. Variation of inverse susceptibility with temperature for $x = 0.5$, 0.6, 0.8, and 1.0 in $Sm_{2-x}Sr_xNiO_{4\pm\delta}$.

constants, respectively. The plots of the $1/\chi$ vs T for selected members of $Pr_{2-x}Sr_xNiO_{4\pm\delta}$ are presented in Fig. 10. The C and Θ values of all the samples were estimated from the linear portions of the graphs in the temperature range 100–300 K. The corresponding μ_{eff} values derived from the Curie constants are listed in Table II together with the theoretically expected moments for Pr^{3+}. The differences in the observed and calculated μ_{eff} values, $\Delta\mu_{eff}$, are also presented in Table II. As shown in Table II, the Weiss constant remains negative for all the compositions, indicating that the dominant exchange interactions are antiferromagnetic. The differences between the observed and calculated (contribution from Pr^{3+} ions) magnetic moments in these compounds may be attributed to the contribution from the Ni^{2+}/Ni^{3+} sublattice and the temperature independent terms.

The temperature dependence of the reciprocal magnetic susceptibilities of the $Sm_{2-x}Sr_xNiO_{4\pm\delta}$ is shown in Fig. 11. The magnetic moments of the orthorhombic compositions in $Sm_{2-x}Sr_xNiO_{4\pm\delta}$ ($x = 0.5$ and 0.6) are localized and exhibit Curie–Weiss behavior in the temperature range 100–300 K. In the case of the tetragonal compositions ($x =$

TABLE II

MAGNETIC PROPERTIES FOR $Pr_{2-x}Sr_xNiO_{4\pm\delta}$ IN THE TEMPERATURE RANGE 100–300 K[a]

Compound	$C_{(obs)}$ emu K/mole	Θ (K)	μ_{eff} (B.M.) observed	μ_{eff} (B.M.)[b] calculated	$\Delta\mu_{eff}$ (B.M.)
$Pr_2NiO_{4.09}$	3.83(4)	−57.6	5.54(3)	5.060	0.48
$Pr_{1.9}Sr_{0.1}NiO_{4.09}$	3.72(3)	−73.7	5.46(2)	4.932	0.53
$Pr_{1.8}Sr_{0.2}NiO_{4.04}$	3.44(2)	−62.4	5.25(2)	4.800	0.45
$Pr_{1.6}Sr_{0.4}NiO_{4.04}$	3.28(1)	−72.6	5.122(8)	4.526	0.596
$Pr_{1.5}Sr_{0.5}NiO_{3.99}$	3.138(9)	−80.1	5.010(7)	4.382	0.628
$Pr_{1.4}Sr_{0.6}NiO_{3.99}$	3.019(1)	−84.4	4.9145(8)	4.230	0.6845
$Pr_{1.2}Sr_{0.8}NiO_{3.99}$	2.545(6)	−78.9	4.512(5)	3.919	0.593
$PrSrNiO_{3.96}$	2.222(5)	−81.3	4.216(5)	3.578	0.638

[a] Data reported here are estimated as per mole of compound.
[b] These values reflect the contribution from Pr^{3+} ions.

0.8 and 1.0) the magnetic moments do not follow the Curie–Weiss law. This nonlocalized magnetic moment probably originates from the mixing of an appreciable fraction of the excited state into the ground state induced by the applied magnetic field, in view of the fact that the $^6H_{7/2}$ excited state is rather close to the $^6H_{5/2}$ ground state in Sm^{3+} ions ($\Delta E \sim 1000\ cm^{-1}$) (*34*). A similar deviation of the Sm^{3+} magnetic moment from the Curie–Weiss law has also been observed in Sm_2CuO_{4-y} (*32*) and $SmCaCuO_3Cl$ (*35*). The Sm^{3+} moments in Sm_2CuO_4 and Gd^{3+} moments in Gd_2CuO_4 order antiferromagnetically at 5.95 and 6.5 K, respectively (*36*), while $SmCaCuO_3Cl$ shows no evidence of magnetic ordering from room temperature down to 2 K (*35*). It appears that the absence of a magnetic order in $Sm_{2-x}Sr_xNiO_{4\pm\delta}$ has the same origin as that of $GdSrNiO_4$ and $SmCaCuO_3Cl$, where it can be attributed to dilution of the paramagnetic moments of the Sm^{3+} and Gd^{3+} ions by the diamagnetic Sr^{2+} ions, which results in a weakening of the correlations between the $4f$ spins.

It is interesting that we did not observe any magnetic contribution from the NiO_2 sublattice to the Gd^{3+} moment in $GdSrNiO_4$. The observed μ_{eff} (7.7 B.M.) derived from the Curie constant (estimated from the temperature range 100–300 K) in $GdSrNiO_4$ is within ~3% of the expected spin-only value (7.94 B.M./Gd^{3+}) for $4f^7$ configuration. The Curie–Weiss temperature, Θ, is −11.9 K. Similar values of μ_{eff} (7.79 B.M./Gd^{3+}) and Θ (−15.3 K) were also observed in Gd_2CuO_{4-y} (*32*).

Conclusion

$Pr_{2-x}Sr_xNiO_{4\pm\delta}$ forms single phase solid solution for $0 \leq x \leq 1.0$. $Ln_{2-x}Sr_xNiO_{4\pm\delta}$ with Ln = Sm, Gd are not stable for x = 0, but K_2NiF_4-type compounds can be stabilized with x = 0.5–1.0 for Sm and x = 1.0 for Gd. These results are consistent with tolerance factor considerations (i.e., $0.86 \leq t \leq 1.0$; $t = (r_A + r_O)/\sqrt{2}\,(r_B + r_O)$), which require a large A cation in stable A_2BO_4 perovskite-related structures. Thus in $Ln_{2-x}Sr_xNiO_{4\pm\delta}$ with Ln = Sm, Gd (smaller A cations relative to Ln = La, Pr, Nd) increasingly larger amounts of Sr substitution in the Ln–O rocksalt layer are required with decreasing size of the rare earth ion.

A structural phase transition from orthorhombic to tetragonal symmetry occurs at $x \sim 0.2$ and 0.8 for $Pr_{2-x}Sr_xNiO_{4\pm\delta}$ and $Sm_{2-x}Sr_xNiO_{4\pm\delta}$, respectively. Within a given solid solution system, at $x = 0.6$, the unit cell parameters exhibit a sharp minimum at a_t and a maximum at c; the tetragonality ratio, c/a_t in a given solid solution thus displays a maximum at $x \sim 0.6$. We have made an attempt to rationalize these anomalies in terms of: (a) the bond competition along the crystallographic c-axis, (b) size effects, (c) a configurational transition from $t_{2g}^6 d_{z^2}^1 d_{x^2-y^2}^0$ to $t_{2g}^6 d_{x^2-y^2}^1 d_{z^2}^0$ at the Ni^{3+} ions, and (d) the Jahn–Teller distortion of Ni^{3+} ion. The lowering of the orthorhombic-to-tetragonal structural phase transition temperature with the incorporation of Sr^{2+} into the LnO sublattice was also observed in the $Pr_{2-x}Sr_xNiO_{4\pm\delta}$ and $Sm_{2-x}Sr_xNiO_{4\pm\delta}$ systems.

The room temperature resistivity (ρ_{RT}) and the activation energy both decrease with increasing Sr content in $Ln_{2-x}Sr_xNiO_{4\pm\delta}$ (Ln = Pr, Sm), demonstrating the influence of the mixed valent nickel ions on the electrical properties. The effect of the mixed valent nickel ions on the electrical transport properties was further illustrated in the high temperature resistivity measurement and the DSC analysis, which showed that the metal–semiconductor transition temperature is progressively lowered with the incorporation of Sr^{2+} into the LnO sublattice. The Seebeck effect indicated that, at room temperature, electrons are the dominant carriers in all the compounds reported here.

In the temperature dependence of the magnetic susceptibility, we see no evidence of long range magnetic ordering in any of the compounds. The absence of long range

magnetic ordering of Sm^{3+} and Gd^{3+} moments in these solid solutions, in contrast to their presence in Sm_2CuO_4 and Gd_2CuO_4, is attributed to the substitution of Sr^{2+} for Ln^{3+} ions. The incorporation of the diamagnetic Sr^{2+} ions dilute the paramagnetic Sm^{3+} and Gd^{3+} ions and suppress the magnetic ordering of $4f$ spins. The absence of magnetic ordering due to Ni–Ni interactions may be related to the "hole doping" effect: if Ni^{3+}, low spin, is present in the structure with empty $d_{x^2-y^2}$ orbitals, an effective Ni^{3+}–Ni^{2+} ferromagnetic interaction competes with the antiferromagnetic interaction of Ni^{2+}–Ni^{2+}, suppressing the cooperative 3D ordering. Alternatively, long range magnetic order of the Ni-sublattice may be obscured by the strong paramagnetism of the rare earth spins.

Because of the anomalous behavior of the lattice parameters and the room temperature resistivity in $Ln_{2-x}Sr_xNiO_{4\pm\delta}$ (Ln = La, Pr, Nd, Sm) at $x = 0.5$, which was attributed to possible charge ordering on the $Ni^{2+/3+}$ site, further structural investigations of $Ln_{2-x}Sr_xNiO_{4\pm\delta}$ (Ln = Pr, Sm) with electron diffraction and transmission electron microscopy methods are in progress.

Acknowledgments

The authors thank Mr. Zeri S. Teweldemedhin and Dr. Robert L. Fuller for their help in the magnetic susceptibility measurements and Mr. Robert Schadd for carrying out the preliminary synthesis. This work was supported by National Science Foundation Solid State Chemistry Grant DMR-90-19301.

References

1. J. G. Bednortz and K. A. Muller, *Z. Phys. B* **61,** 189 (1986).
2. J. B. Goodenough and J. M. Longo, *in* "Landolt-Bornstein Tabellen," Vol. III/49, p. 193 (1970).
3. J. B. Goodenough, *Mater. Res. Bull.* **8,** 423 (1973).
4. J. B. Goodenough and S. Ramasesha, *Mater. Res. Bull.* **17,** 383 (1982).
5. J. M. Bassat, P. Odier, and F. Gervais, *Phys. Rev. B* **35,** 7126 (1987).
6. D. J. Buttrey, J. M. Honig, and C. N. R. Rao, *J. Solid State Chem.* **64,** 287 (1986).
7. C. N. R. Rao, D. J. Buttrey, N. O. Tsuka, P. Ganguly, H. R. Harrison, C. J. Sandberg, and J. M. Honig, *J. Solid State Chem.* **51,** 266 (1984).
8. D. J. Buttrey and J. M. Honig, *J. Solid State Chem.* **72,** 38 (1988).
9. J. D. Jorgensen, B. Debrowski, Shiyou Pei, D. R. Richards, and D. G. Hinks, *Phys. Rev. B* **40,** 2187 (1989).
10. Z. Hiroi, T. Obata, M. Takano, Y. Bando, Y. Takeda, and O. Yamamoto, *Phys. Rev. B* **41,** 11665 (1990).
11. D. J. Buttrey, J. D. Sullivan, G. Shirane, and K. Yamada, *Phys. Rev. B* **42,** 3944 (1990).
12. J. D. Sullivan, D. J. Buttrey, D. E. Cox, and J. Hriljac, *J. Solid State Chem.* **94,** 337 (1991).
13. J. Rodriguez-Carvajal, J. L. Martinez, J. Pannetier, and R. Saez-Puche, *Phys. Rev. B* **38,** 7148 (1988).
14. R. Saez-Puche, J. L. Rodriguez, and F. Fernandez, *Inorg. Chim. Acta.* **140,** 151 (1987).
15. Z. Kakol, J. Spalek, and J. M. Honig, *J. Solid State Chem.* **79,** 288 (1989).
16. J. Gopalakrishnan, G. Colsmann, and B. Reuter, *J. Solid State Chem.* **22,** 145 (1977).
17. Y. Takeda, R. Kanno, M. Sakano, O. Yamamoto, M. Takano, Y. Banndo, H. Akinaga, K. Takita, and J. B. Goodenough, *Mater. Res. Bull.* **25,** 293 (1990).
18. A. B. Austin, L. G. Garreiro, and J. V. Marzik, *Mater. Res. Bull.* **24,** 639, (1989).
19. B. W. Arbuckle, K. V. Ramanujachary, Zhen Zhang, and M. Greenblatt, *J. Solid State Chem.* **88,** 278 (1990).
20. T. Takeda, M. Nishijima, N. Imanishi, R. Kanno, O. Yamamoto, and M. Takano, *J. Solid State Chem.* **96,** 72 (1992).
21. Brian W. Arbuckle, Zhen Zhang, and Martha Greenblatt, *in* "Chemistry of Electronic Ceramic Materials," p. 207 (1990).
22. G. Demazeau, M. Pouchard, and P. Hagenmuller, *J. Solid State Chem.* **18,** 159 (1976).
23. U. Lehmann and Hk. Muller-Buschbaum, *Z. Naturforsch. B* **35,** 389 (1980).
24. Von B. Grande and H. Muller-Buschbaum, *Z. Anorg. Allg. Chem.* **433,** 152 (1977).
25. S.-H. Byeon, G. Demazeau, J. M. Dance, and J.-H. Choy, *Eur. J. Solid State Inorg. Chem.* **28,** 643 (1991).
26. L. M. Zhu, G. Demazeau, M. Pouchard, J. M. Dance, and P. Hagenmuller, *J. Solid State Chem.* **78,** 46 (1989).
27. R. D. Shannon, *Acta Crystallogr. Sect. A: Found. Crystallogr.* **32,** 751 (1976).
28. R. Saez-Puche, R. Fernandez, and W. S. Glaunsinger, *Mater. Sci. Monogr. (React. Solid Pt. A)* **28,** 607 (1985).

29. S. N. RUDDLESDEN AND P. POPPER, *Acta Crystallogr.* **10,** 538 (1957).
30. J. F. ACKERMAN, *Mater. Res. Bull.* **14,** 487 (1979).
31. J. E. GREEDAN, GUO LIU, B. W. ARBUCKLE, K. V. RAMANUJACHARY, AND M. GREENBLATT, *J. Solid State Chem.* **97,** 419 (1992).
32. C. L. SEAMAN, N. Y. AYOUB, T. BJØRNHOLM, E. A. EARLY, S. GHAMATY, B. W. LEE, J. T. MARKERT, J. J. NEUMEIER, P. K. TSAI, AND M. B. MAPLE, *Physica C* **159,** 391 (1989).
33. J. E. GREEDAN AND WENHE GONG, *J. Alloys Comp.* **180,** 281 (1992).
34. R. L. CARLIN, *in* "Magnetochemistry" Chap. 9, Springer-Verlag, New York (1986).
35. R. L. FULLER AND M. GREENBLATT, *J. Solid State Chem.* **92,** 386 (1991).
36. J. D. THOMPSON, S. W. CHEONG, S. E. BROWN, Z. FISK, S. B. OSEROFF, M. TOVAR, D. C. VIER, AND S. SCHULTZ, *Phys. Rev. B* **39,** 6660 (1989).